

Topological properties of curved spacetime extended Su–Schrieffer–Heeger model

Priyanuj Rajbongshi^{1,*} and Ranjan Modak^{1,†}

¹*Department of Physics, Indian Institute of Technology Tirupati, Tirupati 517619, India*

The Su-Schrieffer-Heeger (SSH) model, a prime example of a one-dimensional topologically nontrivial insulator, has been extensively studied in flat space-time. In recent times, many studies have been conducted to understand the properties of the low-dimensional quantum matter in curved spacetime, which can mimic the gravitational event horizon and black hole physics. However, the impact of curved spacetime on the topological properties of such systems remains unexplored. Here, we investigate the curved spacetime (CST) version of the extended SSH model, by introducing a position-dependent hopping parameter. The extended SSH model already exhibits topological phases and the associated phase transitions. Different topological markers suggest that for the same choice of parameters, the CST version of the model retains the imprint of the same topological phases and transitions. Furthermore, the topologically non-trivial phase of the CST model hosts zero-energy edge modes, which are spatially asymmetric in contrast to those of the conventional SSH model. We find that at the topological transition points between phases with different winding numbers, a critical slowdown takes place for zero-energy wave packets near the boundary, indicating the presence of a horizon, and interestingly, if one moves even a slight distance away from the topological transition points, wave packets start bouncing back and reverse direction before reaching the horizon. Moreover, we have also quantified the time scale of the critical slowdown of the wavepacket across different winding-number transition phases. A semiclassical description of the wave packet trajectories also supports these results.

I. INTRODUCTION

One of the most astonishing predictions of Einstein’s theory of general relativity [1] is the potential existence of black holes, i.e., space-time regions from where nothing can escape. From then on, there have been efforts to simulate a black hole horizon and the relevant curve spacetime (CST) physics in the laboratories. In 1981, Unruh proposed a sonic horizon, which is based on the observation that sound waves in flowing fluids, in appropriate conditions, can be described by the same wave equation as a scalar field in a curved space-time. The acoustic horizon occurs if the velocity of the fluid exceeds the speed of sound within the liquid, acting on sound waves exactly as a black hole horizon does [2, 3]. Further, there exist proposals for black hole analogs, analogue Hawking radiation, and other curved spacetime phenomena analogs based on light propagation in dielectric media, liquid Helium 3, and Bose-Einstein condensates, classical electronics circuits, Floquet quantum systems [4–18]. These works have provided a setup for studying the CST physics in laboratories, which has deepened the understanding of the curved spacetime and gravity, e.g., one of the milestones of these studies was to reveal the relation between (1 + 1)D Jackiw-Teitelboim gravity and the Sachdev-Ye-Kitaev model [19–21]. Only in the last few years, there have been some studies that have focused on the condensed matter properties in CST lattice systems, asking extremely fundamental questions like what will happen to the fate of thermalization and localization in CST lattice models [22–25].

On the other hand, one of the main goals of condensed matter physics is to deal with different phases of matter. Traditionally, phase transitions were characterized by order parameters within Landau’s free-energy theory framework and

symmetry breaking. In the past few decades, the identification of new phases of matter that did not break any symmetry, nor could be characterized by the usual order parameters, has led to the appearance of topology in condensed matter systems. While 2D electronic systems, which displayed a quantized Hall conductance [26], are probably 1st known example of such a condensed matter system where topology plays a crucial role, in recent days, a new class of electronic materials such as topological insulators [27–32], topological crystalline insulators [33–35], and topological semimetals [36–39] have emerged as a material having nontrivial Bulk band topology that can be exploited for application in low-power consumption electronic and spintronic devices due to the robustness of their edge states to defects, which are topologically protected. In this context, to understand how these materials behave in realistic situations, it is important to first understand simple toy models that show such a topological phase transition. One such example of a toy model is the one-dimensional (1D) Su-Schrieffer-Heeger (SSH) model, which is an example of a topological insulator [40]. It is a tight-binding model of non-interacting spinless electrons confined in a dimer chain, and has been extensively studied both theoretically and experimentally in the recent past [41–45]. The SSH model was initially introduced to describe a 1D chain of polyacetylene, on which electrons hop with staggered hopping amplitudes. There are two sites in each unit cell of this model; thus, it is a two-band model, and has winding number as its corresponding topological invariant. In particular, the number of edge states on a boundary of the system has a one-to-one correspondence to the winding number associated with this model.

In this work, our main goal is to connect these two extremely different branches of physics, 1) curved spacetime and black hole, and 2) topological systems in condensed matter. We propose a CST lattice model inspired by the two-band extended SSH models. First, we investigate whether we can see the event horizon physics or not. Next, we investigate whether the CST version of the extended SSH models has a

* ph24d004@iittp.ac.in

† ranjan@iittp.ac.in

topologically non-trivial phase or not. Remarkably, we answer both questions affirmatively in this manuscript. We show using different topological markers that the CST-SSH model and its extended version also show a topological phase transition. Most interestingly, exactly at the transition point, a critical slowdown takes place for zero-energy wave packets, which indicates the presence of a horizon.

This paper is organized as follows: We define our CST-SSH models in Section II. Section III shows the wave packet dynamics and semi-classical analysis of the dynamics. We investigate the gap of the spectrum and also the zero-energy states in Sec. IV. We dedicate the Sec. V for different topological markers to check the topological nature of the models. Section. VI shows the effect of quench across different topological phases in CST-SSH. We then quantify the slowdown parameter in Sec. VII for the extended CST-SSH. Finally, we summarize our findings in Sec. VIII.

II. CURVED SPACETIME SSH MODELS

In some recent studies [25, 46], an equivalence between the Dirac equation in curved spacetime and a tight-binding condensed matter system with power law position-dependent hopping has been demonstrated. As suggested, we can establish a direct connection between the continuum field theory and a condensed matter system by considering a simple tight-binding Hamiltonian in real space with nearest-neighbor (nn) position-dependent hopping:

$$\mathcal{H} = - \sum_{n=1}^{N-1} t_n (c_n^\dagger c_{n+1} + h.c.), \quad (1)$$

where c_n^\dagger and c_n are fermionic-creation and annihilation operators, and t_n is a position-dependent hopping parameter. If $t_n = t$ (the nn hopping amplitude is constant for all sites), then the Hamiltonian can be diagonalized very easily in the momentum space k . The Hamiltonian will read as, $\mathcal{H} = \sum_k \varepsilon(k) c_k^\dagger c_k$, where c_k^\dagger and c_k are creation and annihilation operators in momentum space, and $\varepsilon(k) = -2t \cos k$. In case of position-dependent hopping $t_n (\approx t (\frac{n}{N})^\sigma)$, and in the limit $N \rightarrow \infty$, the difference between the two adjacent hopping amplitudes, $t_{n+1} - t_n = t \left[(x + \frac{1}{N})^\sigma - (x)^\sigma \right]$, where, $x = \frac{n}{N}$.

Now, the 1st term, in the limit Nx large, read as $\left(x + \frac{1}{N}\right)^\sigma = x^\sigma \left(1 + \frac{\sigma}{Nx} + \mathcal{O}\left(\left(\frac{1}{Nx}\right)^2\right)\right)$. Therefore, $(t_{n+1} - t_n) \approx t \left(\frac{x^{\sigma-1} \sigma}{N}\right)$. Thus, in the thermodynamic limit, $N \rightarrow \infty$ and for the bulk, i.e., $n \gg 0$, the hopping variation in neighboring sites is effectively negligible, i.e. for a short segment of the lattice, the hopping is effectively constant. Thus, we can approximate the local band structure for the bulk as $\varepsilon(n, k) \sim -2t_n \cos k$, and the local Fermi velocity as $v_F(n) \sim \pm 2t_n$. Thus, the local velocity varies with spatial coordinates, as the hopping here is position-dependent. In the continuum limit, these kinds of lattice models are equivalent to a massless Dirac field with the two-component spinor $\Psi = (\psi_+, \psi_-)^T$ that obeys the follow-

ing time-evolution equation [46],

$$\partial_\tau \Psi = \Sigma_3 \left(v(x) \partial_x + \frac{1}{2} \frac{dv}{dx} \right) \Psi, \quad (2)$$

where, Σ_i , ($i = 1, 2, 3$) are the Pauli matrices and $v(x)$ is a position-dependent velocity, relating to the hopping as $v(x) = 2t(x)$. It is identical to the Dirac equation on (1+1) D spacetime in the massless limit. Thus, Eq. 1 is the low-energy discrete version of a Dirac Hamiltonian in the continuum limit with the equation of motion 2, and with the Rindler metric

$$ds^2 = -v^2(x) d\tau^2 + dx^2. \quad (3)$$

At $v(x) = 0$, i.e., $t(x) = 0$, this Rindler metric possesses an event horizon, as at that point, the local speed of light goes to zero. If we let $t(x) \propto x^\sigma$, where σ is indicating the warping of spacetime [22], equivalently, in the lattice model (1) $t_n = \left(\frac{n}{N-1}\right)^\sigma$, at $n/N \rightarrow 0$ limit, the lattice model will possess event horizon for $\sigma \geq 1$: an gaussian wave-packet propagating in this lattice will suffer eternal slowdown and never reaches the origin, thus effectively forming an event horizon at the origin in the lattice model.

In a similar spirit, in this work, we investigate whether we observe the horizon physics in a two-band topological system with next nearest neighbor hopping, and what would happen to the topological characteristics after introducing position dependent hopping. Hence, we study an extended version of the SSH model, where the hopping is not just restricted to between nearest neighbors, but higher-order hopping has also been allowed. In the context of the standard SSH model, a similar model was studied in Ref. [47, 48], known as the extended SSH model. Here we study the CST version of such models, where hopping is position-dependent, and the model reads as,

$$\begin{aligned} H = & \sum_{n=1}^N t_1(n) c_{n,A}^\dagger c_{n,B} + \sum_{n=1}^{N-1} t_2(n) c_{n,B}^\dagger c_{n+1,A} \\ & + t_3(n) c_{n,A}^\dagger c_{n+1,B} + \sum_{n=1}^{N-2} t_4(n) c_{n,B}^\dagger c_{n+2,A} + h.c., \end{aligned} \quad (4)$$

where $c_{n,A}^\dagger$, $c_{n,A}$ ($c_{n,B}^\dagger$, $c_{n,B}$) are fermionic creation and annihilation operators at the A sub-lattice (B sub-lattice) of the nth unit cell, and, $t_1(n) = t_1 \left(\frac{2n-1}{2N-1}\right)^\sigma$, $t_2(n) = t_2 \left(\frac{2n}{2N-1}\right)^\sigma$ are the nearest neighbor intracellular and intercellular position-dependent hoppings, and, $t_3(n) = t_3 \left(\frac{2n-1}{2N-1}\right)^\sigma$, $t_4(n) = t_4 \left(\frac{2n}{2N-1}\right)^\sigma$. For $\sigma = 0$, the Hamiltonian will have translational invariance. Hence, it can be fourier transformed to momentum k space, where the winding number transition can happen when the components of the bloch vector becomes zero, i.e., $d_x(k) = t_1 + (t_2 + t_3) \cos k + t_4 \cos 2k$ and, $d_y(k) = (t_2 - t_3) \sin k + t_4 \sin 2k$ both becomes 0, which gives us conditions:

$$\begin{aligned} t_1 + t_2 + t_3 + t_4 &= 0, \\ t_1 - (t_2 + t_3) + t_4 &= 0, \\ t_4(t_1 - t_4) + t_3(t_3 - t_2) &= 0. \end{aligned} \quad (5)$$

at gap closing momentum $k_c = 0, \pi$ and for k_c satisfying $\cos k_c = \frac{t_3 - t_2}{2t_4}$; ($t_4 \neq 0, |\frac{t_3 - t_2}{2t_4}| \leq 1$), respectively, where we can observe winding number transitions. To gain insight into the topological properties, we also consider a limiting case of the Hamiltonian 4, with $t_3 = t_4 = 0$, which can be considered as the curved-space-time version of the standard SSH model.

III. WAVE-PACKET VS SEMICLASSICAL DYNAMICS

The first question we try to address here is whether we see any event horizon physics for the Hamiltonian Eq. (4). Hence, we first study the wave-packet dynamics. In this section, we study the wave packet dynamics under the CST-SSH Hamiltonian of a Gaussian wave packet and compare the results with the semiclassical set of coupled differential equations that govern wave packet trajectories. We consider the following Gaussian wave packet,

$$\psi(x, \tau = 0) = \frac{1}{\sqrt{4\pi\omega^2}} e^{-\frac{1}{2}\left(\frac{x-x_0}{\omega}\right)^2} e^{ip_0x}, \quad (6)$$

which describes a normalized gaussian wave packet at time $\tau = 0$ centered at position x_0 of the lattice, and having initial momentum of p_0 , ω is the width of the wave packet. We observe that, for the parameter values satisfying any of the conditions at Eq. 5, the wavepacket having the initial momentum of $p_0 = k_c/2$ suffers a critical slowdown down while approaching towards the origin, and, never returns (Figs.1a, 1b), for $\sigma \geq 1$. On the other hand, for any other combinations of (t_1, t_2, t_3, t_4) , it comes back before reaching the origin 1c, which we identify as a ‘turning point’. This x_{\min} depends on the details, e.g., initial momentum p_0 , the Hamiltonian parameters σ, t_1, t_2, t_3 , and t_4 . In case of the CST version of the standard SSH, we find that if $t_1 \neq t_2$, the wave-packet first propagates towards an edge and then returns from some point x_{\min} , and, for $t_1 = t_2$ and $p_0 = -\pi/2$, it eternally slows down while evolving as it approaches the edge $x = 0$, and never returns. We can identify it as the asymptotic localization of wave packets at the origin, which mimics the key feature expected for wave packet dynamics in the presence of an event horizon.

A. Semiclassical dynamics for the Extended CST-SSH model

We can dive deeper into the time evolution of the wave packet by obtaining the semiclassical trajectories of the Hamiltonian of the extended version of the CST-SSH model. For a position-dependent extended SSH model, the two recursive energy eigenvalue equations can be written as,

$$t_4(n-2)\psi_{B,n-2} + t_2(n-1)\psi_{B,n-1} + t_1(n)\psi_{B,n} + t_3(n)\psi_{B,n+1} = \varepsilon\psi_{A,n} \quad (7)$$

$$t_3(n-1)\psi_{A,n-1} + t_1(n)\psi_{A,n} + t_2(n)\psi_{A,n+1} + t_4(n)\psi_{A,n+2} = \varepsilon\psi_{B,n} \quad (8)$$

Following the reference [46], we introduce continuous function $\tilde{\psi}_{A/B}(x_n)$ which is related to the discrete $\psi_{A/B,n}$ of the lattice model as: $\tilde{\psi}_{A/B}(x_n) = \psi_{A/B,n}$, where, $x_n = \frac{n}{N-1}$ is the position of the n -th unit cell in the conituum space, with $\tilde{\psi}_A(x_n) - \tilde{\psi}_B(x_n) = \delta x = \frac{1}{2N-1}$, the minimum distance on the lattice. Expanding the wave functions in Taylor series, we get a mapping between the discrete $\psi_{A/B,n\pm 1}$ with continuous $\tilde{\psi}_{A/B}(x_n)$ as $\psi_{A/B,n\pm 1} = e^{\pm i2\delta x \hat{p}} \tilde{\psi}_{A/B}(x_n)$. The factor of two comes as changing the unit cell from n to $n \pm 1$ corresponds to moving $2\delta x$ in space to the right or left, and the minimum length scale on the lattice is δx . We then end up with the following pairs of equations,

$$\begin{aligned} & \left(t_4(\hat{x} - 4\delta x)e^{-4i\delta x \hat{p}} + t_3(\hat{x})e^{2i\delta x \hat{p}} \right. \\ & \left. + t_2(\hat{x} - 2\delta x)e^{-2i\delta x \hat{p}} + t_1(\hat{x}) \right) \tilde{\psi}_B(x, \tau) = i \partial_\tau \tilde{\psi}_A(x, \tau) \end{aligned} \quad (9)$$

and,

$$\begin{aligned} & \left(t_4(\hat{x})e^{4i\delta x \hat{p}} + t_3(\hat{x} - 2\delta x)e^{-2i\delta x \hat{p}} \right. \\ & \left. + t_2(\hat{x})e^{2i\delta x \hat{p}} + t_1(\hat{x}) \right) \tilde{\psi}_A(x, \tau) = i \partial_\tau \tilde{\psi}_B(x, \tau) \end{aligned} \quad (10)$$

where, $\tilde{\psi}_{A/B}(x, \tau) = \tilde{\psi}_{A/B}(x)e^{-ie\tau}$. Combining the two equations, we get the continuum Hamiltonian as a 2×2 matrix

$$\tilde{H} = \begin{pmatrix} 0 & T(\hat{x}, \hat{p}) \\ T^*(\hat{x}, \hat{p}) & 0 \end{pmatrix},$$

where, $T(\hat{x}, \hat{p}) = t_1(\hat{x}) + e^{-2i\delta x \hat{p}} t_2(\hat{x}) + t_3(\hat{x})e^{2i\delta x \hat{p}} + e^{-4i\delta x \hat{p}} t_4(\hat{x})$, which acts on the spinor $\Psi(x, \tau) = \begin{pmatrix} \tilde{\psi}_A(x, \tau) \\ \tilde{\psi}_B(x, \tau) \end{pmatrix}$. Now, neglecting the commutation relation between \hat{x} and \hat{p} , and then, rescaling the momentum and time as $p \rightarrow p/\delta x$ and $\tau \rightarrow \tau/\delta x$, we could express the energy as follows, and with it, we can obtain the equation of motion. The semiclassical equations of motion (in one dimension) read:

$$\dot{x} = \frac{\partial E_\pm}{\partial p}, \quad \dot{p} = -\frac{\partial E_\pm}{\partial x}. \quad (11)$$

Here, The energy expression,

$$E_\pm(x, p) = \pm |T(x, p)| = \pm \sqrt{T_R^2(x, p) + T_I^2(x, p)},$$

where, $T_R = t_1(x) + (t_2(x) + t_3(x))\cos(2p) + t_4(x)\cos(4p)$ and $T_I(x, p) = (t_3(x) - t_2(x))\sin(2p) - t_4(x)\sin(4p)$ are the real and imaginary part of $T(x, p)$. Now, after substituting the values of T_R and T_I , one can obtain the equations of motion as:

$$\dot{x} = \pm \frac{1}{\sqrt{T_R^2(x, p) + T_I^2(x, p)}} (T_R \partial_p T_R + T_I \partial_p T_I) \quad (12)$$

$$\dot{p} = \mp \frac{1}{\sqrt{T_R^2(x, p) + T_I^2(x, p)}} (T_R \partial_x T_R + T_I \partial_x T_I), \quad (13)$$

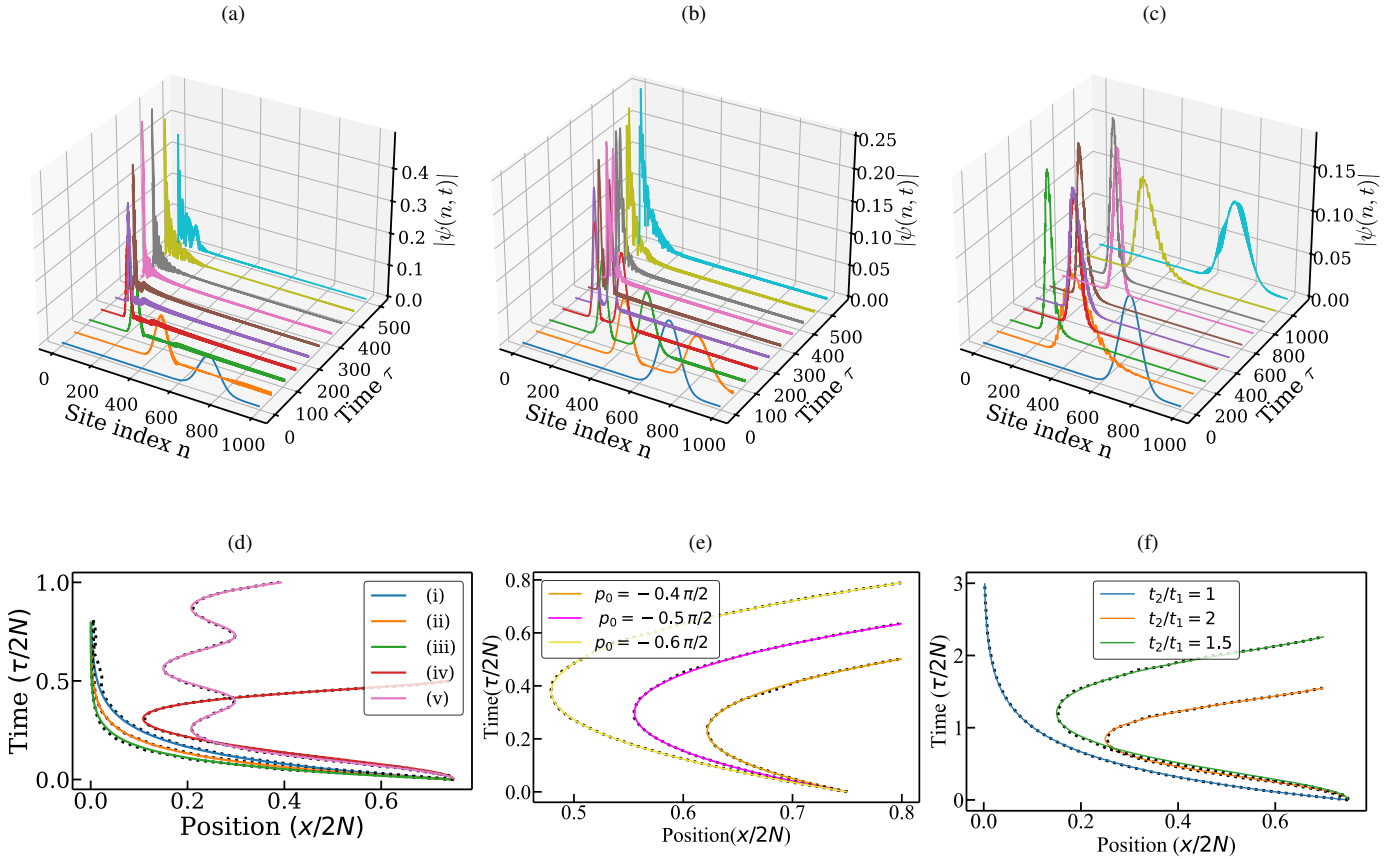


FIG. 1: Time evolution of Gaussian wave packet in the Extended CST-SSH Hamiltonian of system size $2N = 1000$ (500 unit cells) with $\sigma = 1$, $\omega = 50$, $x_0 = 750$: (a) obeying the relation $t_1 - (t_2 + t_3) + t_4 = 0$ with hopping $(t_1, t_2, t_3, t_4) = (3, -2, 1, -4)$, with $|p_0| = \pi/2$, (b) obeying the relation $t_1 + t_2 + t_3 + t_4 = 0$ with hopping $(t_1, t_2, t_3, t_4) = (0, 1, 1, -2)$, at $|p_0| = \pi$ (c) extended CST-SSH having winding no 2, with hopping parameters $(t_1, t_2, t_3, t_4) = (0, 1, 1, -3)$ at $|p_0| = \pi$ (d) peak position vs. time for different combinations of hopping and initial momentum $(t_1, t_2, t_3, t_4, p_0)$: (i) $(0, 1, 1, -2, \pi)$, (ii) $(3, -2, 1, -4, \pi/2)$, (iii) $(3, 1, 1, 3, \pi/4)$ (iv) $(3, -2, 1, -3, \pi/2)$, and, (v) $(0, 1, 1, -3, \pi)$. (i), (ii) and (iii) suffer eternal slowdown; whereas, (iv) and (v) return before reaching the origin. For $\sigma = 1$, $\omega = 25$, $x_0 = 750$: (e) peak position of the Gaussian wave packet vs. time for different p_0 , at $\sigma = 1$, having $(t_1, t_2, t_3, t_4) = (1, 1.9, 0, 0)$; (f) peak position vs. time for different t_1/t_2 ratios with $(t_3, t_4) = (0, 0)$ at $p_0 = -\pi/2$. Dotted lines are numerical; solid lines are semiclassical predictions.

where, ∂_p and ∂_x are the partial derivatives with respect to p and x , respectively. Here, the \mp signs just indicate the direction of the propagation of the trajectories. Fig. 1d shows the comparison between the numerical time evolution (dotted black lines) and the semiclassical equations of motion (colored lines) to obtain the peak positions of the wave packets at various times for different hopping parameters. The semiclassical calculations show excellent agreement with the numeri-

cal time evolution of the Gaussian wavepackets. Semiclassical trajectories can also allow us to predict the turning point. One can analytically obtain the turning point by taking the conserved nature of the average energy of wave packet from the semiclassical calculation. One can obtain the analytical value of the turning point by equating the energy expression at (x_0, p_0) and at (x_{\min}, p) , where choosing an appropriate p makes $\dot{x} = 0$. For $p = 0$, the turning position reads as:

$$x_{\min} = x_0 \left[\frac{(t_1 + (t_2 + t_3) \cos 2p_0 + t_4 \cos 4p_0)^2 + ((t_3 - t_2) \sin 2p_0 - t_4 \sin 4p_0)^2}{(t_1 + t_2 + t_3 + t_4)^2} \right]^{\frac{1}{2\sigma}} \quad (14)$$

In Eq. (14), the expression in the numerator is exactly the

squared band energy of the corresponding homogeneous ex-

tended SSH chain evaluated at momentum p_0 , while the denominator is the squared band energy at $k = 0$. Equation (14) has been derived by equating the energy at (x_0, p_0) and at (x_{\min}, p) , and then choosing $p = 0$ so that the semiclassical velocity $\dot{x} = \partial_p E(x, p)$ vanishes at the turning point. We have also assumed $(t_1 + t_2 + t_3 + t_4) \neq 0$, so that the denominator remains finite and the turning point is determined entirely by the value of the numerator. For fixed hopping amplitudes and fixed x_0 , the turning position x_{\min} is therefore controlled by how large the homogeneous band energy at the initial momentum p_0 is: when this energy decreases, the numerator of Eq. (14) becomes small and the packet penetrates deeper; when the numerator vanishes, x_{\min} becomes zero.

The condition that the numerator of Eq. (14) is zero is precisely the bulk gap closing condition of the homogeneous extended SSH model evaluated at the initial momentum p_0 . This can be seen explicitly in, for example, at $|p_0| = \pi/2$, we have the numerator becomes $(t_1 - (t_2 + t_3) + t_4)^2$, and $x_{\min} = 0$ occurs when $t_1 - (t_2 + t_3) + t_4 = 0$, which is the band closing at $k = \pi$. Finally, for a generic critical momentum $p_0 = p_c$, the condition $x_{\min} = 0$ requires the numerator of Eq. (30) to vanish. Since this numerator is a sum of two squares, both terms must vanish simultaneously. This yields $t_4(t_1 - t_4) + t_3(t_3 - t_2) = 0$, with $\cos(2p_c) = \frac{t_3 - t_2}{2t_4}$, which is precisely the finite-momentum gap-closing condition of the extended SSH chain, with $k_c = 2p_c$.

More generally, Eq. (14) is just one branch of the turning point obtained by choosing $p = 0$ at the turning position. The semiclassical condition $\dot{x} = \partial_p E(x, p) = 0$ can, however, be satisfied at other values of p as well. For example, at $p = \pi/2$ the group velocity of the homogeneous extended SSH band also vanishes, and repeating the same steps gives an analogous expression for x_{\min} in which the denominator is the squared band energy at $k = \pi$, namely $(t_1 - t_2 - t_3 + t_4)^2$, while the numerator remains the same function of p_0 as in Eq. (14), which one might use in case of $(t_1 + t_2 + t_3 + t_4) = 0$. at $p_0 = 0$, in this expression, the numerator reduces to $(t_1 + t_2 + t_3 + t_4)^2$, and we obtain $x_{\min} = 0$ when $(t_1 + t_2 + t_3 + t_4) = 0$, which is the band closing at $k = 0$. Thus, all the bulk gap closing conditions at Eq.5 of the extended SSH model can be recovered consistently from the turning point expression by demanding that the numerator of Eq. (14) vanishes at suitable initial momenta p_0 . In the present work, we use Eq. (14) as a convenient representative branch to illustrate how the extended CST-SSH dynamics encodes the three bulk gap closing constraints through the dependence of x_{\min} on the hopping amplitudes and the initial momentum p_0 .

Thus, we find that the gap-closing conditions for homogeneous extended SSH models, which determine the topological transitions between different winding numbers, also correspond to the conditions under which x_{\min} becomes zero in the extended CST-SSH model. This indicates that horizon physics in the extended CST-SSH model emerges only at those parameter values where topological phase transitions occur in the homogeneous extended SSH model.

In a similar spirit to the previous calculations, we can analyze the semiclassical dynamics for the CST version of the standard SSH Hamiltonian, the limiting case of Eq. 4 with

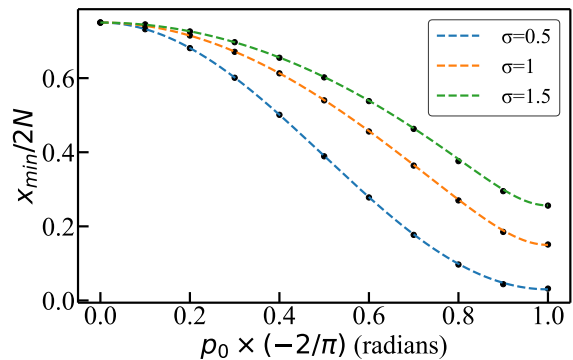


FIG. 2: Plotting of turning point by numerical calculation (black dotted lines) and from semiclassical formula 17 (colored dashed lines) at different initial momenta p_0 for different values of σ , at $(t_1, t_2, t_3, t_4) = (1, 1.5, 0, 0)$, for system size $2N = 1000$ (500 unit cells),

$t_3 = t_4 = 0$. After obtaining the recursive energy eigenvalue equations and the continuum Hamiltonian, we can obtain the semiclassical equation of motion as:

$$\dot{x} = \frac{\partial E_{\pm}}{\partial p} = \mp \frac{2t_1(x)t_2(x)\sin(2p)}{\sqrt{t_1^2(x) + t_2^2(x) + 2t_1(x)t_2(x)\cos(2p)}} \quad (15)$$

$$\begin{aligned} \dot{p} &= -\frac{\partial E_{\pm}}{\partial x} \\ &= \mp \frac{t_1(x)t_1'(x) + t_2(x)t_2'(x) + \cos(2p)(t_1'(x)t_2(x) + t_1(x)t_2'(x))}{\sqrt{t_1^2(x) + t_2^2(x) + 2t_1(x)t_2(x)\cos(2p)}} \end{aligned} \quad (16)$$

In Figs. 1e and 1f, the semi-classical trajectories are compared with the peak position of exact dynamics results. Moreover, the semiclassical result can also mimic the event horizon physics for $t_1 = t_2$ and $p_0 = -\pi/2$. With $t_1 = t_2$, the Hamiltonian matrix essentially becomes identical with the CST-TB Hamiltonian [25], in other words, it can also be referred to as the topological transition point of the usual SSH model. Semiclassical equations can similarly allow us to predict the turning point x_{\min} for $p_0 \neq -\pi/2$,

$$x_{\min} = x_0 \left[\frac{t_1^2 + t_2^2 + 2t_1 t_2 \cos(2p_0)}{(t_1 + t_2)^2} \right]^{\frac{1}{2\sigma}} \quad (17)$$

Figure. 2 shows how the turning point varies with different p_0 values at different σ . The numerical and analytical turning points are extremely well lined up, solidifying the validity of semiclassical calculations. Moreover, the equation suggests that for x_{\min} to be zero, the two hopping t_1 and t_2 must be equal, leading to a more simplified expression $x_{\min} = x_0 (\cos p_0)^{\frac{1}{\sigma}}$, when $p_0 = \pm\pi/2$, only then x_{\min} becomes 0. Hence, in the case of $t_1 \neq t_2$, the wave packet has no initial momentum p_0 value for which the turning point becomes 0. It

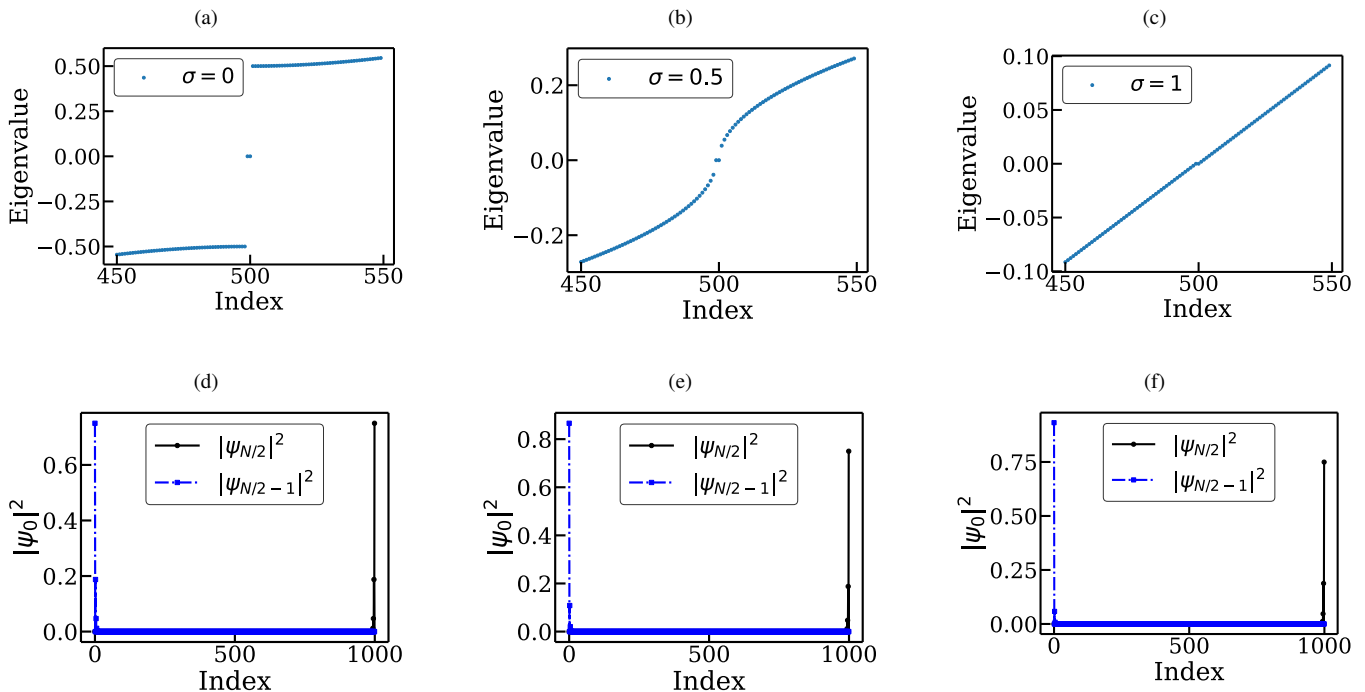


FIG. 3: Closing of the energy band gap and variation of zero energy eigen states variation with σ : for a system size $2N = 1000$ (500 unit cells) with $(t_1, t_2, t_3, t_4) = (0.5, 1, 0, 0)$. Top row (a)–(c): Eigenvalue spectra for $\sigma = 0, 0.5$, and 1 respectively. Bottom row (d)–(f): Corresponding zero-energy eigenstates profiles.

also validates our previous numerical finding, i.e., only when $t_1 = t_2$, the model can show the synthetic horizon effect, and that too for $p_0 = -\pi/2$, which also has been observed for the tight binding lattice model [22, 25, 46].

IV. ANALYTICAL EXPRESSION FOR THE EXACT ZERO ENERGY EIGENFUNCTIONS

From the wave-packet dynamics, it is apparent that the extended CST-SSH model can also mimic horizon physics for certain choices of parameters. This naturally raises the question of whether this model also exhibits a topological phase transition. Note that in the $\sigma = 0$ limit, this model reduces to the usual extended SSH model, which undergoes a topological phase transition between a topologically trivial phase and a topologically non-trivial phase. In the topologically non-trivial phase, under open-boundary conditions, zero-energy states appear that are localized at the two edges of the system. An immediate question then arises: what happens to these edge states when $\sigma > 0$? In particular, do such edge states survive in the presence of the CST deformation? In the following, we analyze this question. For analytical simplicity, we restrict our discussion to the CST-SSH model; however, the analysis can be straightforwardly extended to the extended CST-SSH model.

First, we perform a numerical check in Fig. 3. Figures in

the lower panel suggest that zero energy states still survive for finite σ , though the upper panel figures showing gap is becoming smaller with increasing σ . Moreover, those states remain localized at the edges. However, unlike the usual SSH model, the states are asymmetric; the left edge state seems to become more localized compared to the right edge state with increasing σ .

It is reasonably straightforward to obtain those zero eigenstates by solving the time-independent Schrödinger equation for the CST-SSH Hamiltonian, and one can easily obtain two recursive relations for two sub-lattices A and B.

For sublattice A:

$$t_2(n-1)\psi_{B,n-1} + t_1(n)\psi_{B,n} = 0 \quad (18)$$

For sublattice B:

$$t_1(n)\psi_{A,n} + t_2(n)\psi_{A,n+1} = 0 \quad (19)$$

Now, from (18),

$$\begin{aligned} \psi_{B,n} &= -\frac{t_1(n+1)}{t_2(n)}\psi_{B,n+1} \\ &= \left(-\frac{t_1(n+1)}{t_2(n)}\right)\left(-\frac{t_1(n+2)}{t_2(n+1)}\right)\cdots\left(-\frac{t_1(N)}{t_2(N-1)}\right)\psi_{B,N} \\ &= \left(-\frac{t_1}{t_2}\right)^{N-n} \prod_{m=n+1}^N \left(\frac{2m-1}{2(m-1)}\right)^\sigma \psi_{B,N} \end{aligned} \quad (20)$$

Likewise, for sublattice B, we can obtain from (19),

$$\begin{aligned}\psi_{A,n} &= -\frac{t_1(n-1)}{t_2(n-1)}\psi_{A,n-1} \\ &= \left(-\frac{t_1}{t_2}\right)^{n-1} \prod_{m=1}^{n-1} \left(\frac{2m-1}{2m}\right)^\sigma \psi_{A,1}\end{aligned}\quad (21)$$

These two zero-energy eigenstates $\psi_{A,n}$ and $\psi_{B,n}$ will appear on the left and right edges of the chain, respectively. $\psi_{B,N}$ and $\psi_{A,1}$ can easily be obtained by normalizing the eigen states. For the standard SSH model, with $\sigma = 0$, both states are identical, only one is peaked at the left edge, and the other at the right. But with the introduction of σ , asymmetry arises. The state on the right edge remains almost the same for non-zero σ , and the peak height on the left edge keeps increasing with σ . Figure 4 shows how the right-to-left peak ratio of probability densities varies with σ , showing exact matching with the ratio calculation from the analytical expression.

Another thing to note is the closing of the energy gap (ΔE) with σ . We observe that the gap gradually closes with increasing σ and becomes almost non-existent as σ reaches 1. Such gaplessness in topological insulator due to inhomogeneity or disorder has also been observed in the literature [49–51]. From Fig. 5, we observed that ΔE decreases with σ as $\Delta E \propto N^{-\sigma}$ for a fixed t_1, t_2, t_3, t_4 . Note that the finite-size system on the lattice will always have a gap, and a typical gap between two adjacent energy eigenvalues decreases with system size as N^{-1} (we have found the same for our model as well). Thus, the ratio between ΔE and the typical gap in the spectrum scales as $N^{1-\sigma}$, indicating the presence of isolated zero-energy states even for non-zero $\sigma < 1$. The fact that $N\Delta E$ increases with N , suggests the system remains gapped even in the thermodynamic limit for $\sigma < 1$ [52], and gapless for $\sigma \geq 1$ (see Fig. 5 and also Appendix A). This observation indicates that for any combination of t_1, t_2, t_3, t_4 , even if the parameters do not correspond to a topological phase transition point, the system becomes gapless in the $\sigma \geq 1$ region. However, in this regime we do not observe horizon physics. Hence, the presence of a gapless spectrum alone does not guarantee the occurrence of a critical slowdown. Furthermore, unlike the standard SSH model, the extended SSH model cannot, at the topological transition points, be mapped onto a single-band tight-binding CST Hamiltonian. Nevertheless, we also observe well-localized zero-energy edge states for the σ higher than 1 as well.

V. TOPOLOGICAL SIGNATURES

In the previous section, the survival of the zero-energy edge states for $\sigma > 0$ shows the signature that the CST version of the SSH model can retain the imprint of the same topological phases and transition of the usual SSH models. However, the CST-SSH models remain gapless for $\sigma \geq 1$. In order to understand that further, one needs to understand the symmetries of the model, as well as some proper topological markers, which

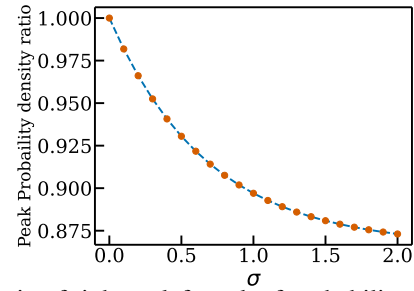


FIG. 4: Ratio of right-to-left peak of probability densities vs σ for a system size $2N = 1000$ (500 unit cells) with $(t_1, t_2, t_3, t_4) = (0.5, 1, 0, 0)$. Here the dotted lines represent the numerical calculations and the dashed lines are from the analytical expressions of the zero energy eigenstates 21,20

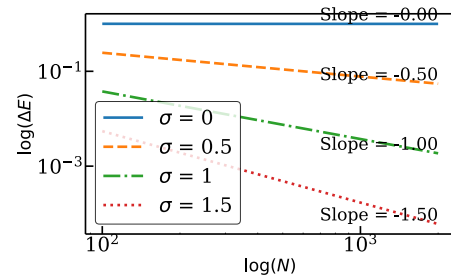
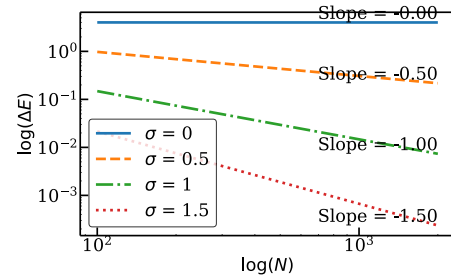


FIG. 5: Energy gap ΔE at various system size N for different σ , for the Extended CST-SSH with $(t_1, t_2, t_3, t_4) = (2, 1, -1, -4)$ (top), and, for $(t_1, t_2, t_3, t_4) = (0.5, 1, 0, 0)$ (bottom)

are required. First, we investigate whether even after the introduction of warping of spacetime (σ), the Hamiltonian will still remain in the BDI category with winding number as its topological invariant quantity, as it is observed for the usual SSH model. Since the position-dependent hopping terms are real, the time reversal operator acting on the Hamiltonian $\hat{T}\hat{H}\hat{T}^{-1} = H$ leaves it invariant. Moreover, the Hamiltonian being a spinless fermionic system, $\hat{T}^2 = \mathbb{I}$. For chiral symmetry, first, we define $\hat{\Gamma}_A = \sum_{n=1}^N c_{n,A}^\dagger c_{n,A}$ and $\hat{\Gamma}_B = \sum_{n=1}^N c_{n,B}^\dagger c_{n,B}$ as projectors on sublattice A and B [53]. Then, the chiral operator is defined by $\hat{\Gamma} = \hat{\Gamma}_A - \hat{\Gamma}_B$, which anti-commutes with the Hamiltonian $\hat{\Gamma}\hat{H}\hat{\Gamma} = -H$, since the bipartite nature is maintained in the modified position-dependent SSH models. This anti-commutation relation holds regardless of the position-dependent nature of the hopping amplitudes [53]. Time re-

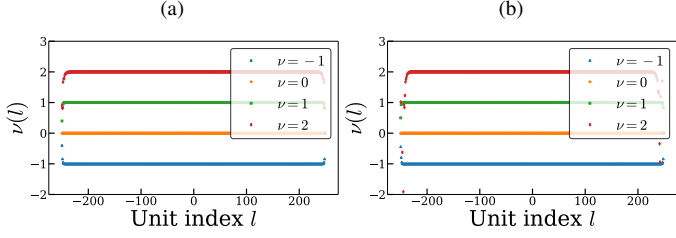


FIG. 6: Local Topological Marker (LTM) for extended CST-SSH model (a) $\sigma = 0$ and (b) $\sigma = 1$, for the CST-SSH model having system size $2N = 1000$ (500 unit cells), giving the same winding numbers for both σ values. $(t_1, t_2, t_3, t_4) = (0.5, 0, 1, 0), (1, 0.5, 0, 0), (0.5, 1, 0, 0), (0, 1, 1, -3)$ are chosen to obtain winding numbers $-1, 0, 1, 2$, respectively.

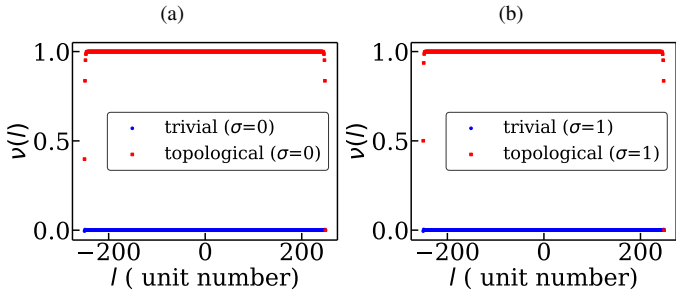


FIG. 7: Local Topological Marker (LTM) for (a) $\sigma = 0$ and, (b) $\sigma = 1$ for trivial $(t_1, t_2, t_3, t_4) = (1, 0.5, 0, 0)$ and topological phase $(t_1, t_2, t_3, t_4) = (0.5, 1, 0, 0)$, for the CST-SSH model having system size $2N = 1000$ (500 unit cells)

versal and Chiral symmetry being present with $T^2 = \Gamma^2 = \mathbb{I}$, we can combine them as, $\hat{C} = \hat{T}\hat{\Gamma}$, which can acts as a particle hole symmetry, i.e., an anti-unitary operator that anti-commutes with the Hamiltonian, and also $\hat{C}^2 = \mathbb{I}$. Thus, the CST-SSH Hamiltonians remain in the BDI category in the Altland-Zirnbauer tenfold classification of topological insulators and superconductors [54, 55] with an integer \mathbb{Z} topological invariant like its standard counterpart in the usual SSH model. Therefore, the symmetries remain invariant under the position-dependent hopping amplitude, and so does the topological invariant, i.e., winding number. However, in the CST-SSH models, the absence of translational symmetry prevents us from utilizing the k-space to calculate the winding number. Therefore, we adopt two real space markers to calculate the topological invariants: (i) Local topological marker (LTM), (ii) Mean chiral displacement (MCD).

A. Local Topological Marker

For a dimer chain with broken translational symmetry, the Local Topological Marker (LTM) can give the value of the

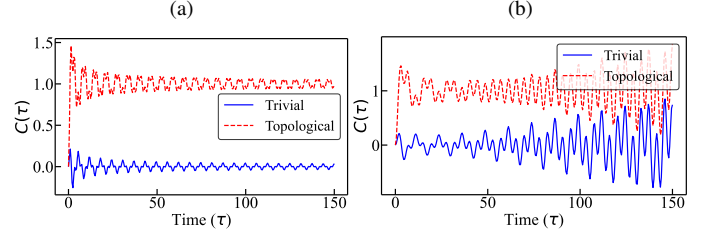


FIG. 8: Time dependent MCD for both topological (red) with $(t_1, t_2, t_3, t_4) = (0.5, 1, 0, 0)$ and trivial (blue) with $(t_1, t_2, t_3, t_4) = (1, 0.5, 0, 0)$ for (a) $\sigma = 0$ and, (b) $\sigma = 1$ for system size $2N = 1000$ (500 unit cells)

topological invariant quantity in its bulk. We here obtain the winding number in real space using LTM [56, 57]. It is based on the rearranged eigenfunctions corresponding to the ascending eigenvalues. The Local topological Marker(LCM) can be defined as:

$$v(l) = \frac{1}{2} \sum_{a=A,B} \{ (\mathbb{Q}_{BA}[\mathbb{X}, \mathbb{Q}_{AB}])_{la,la} + (\mathbb{Q}_{AB}[\mathbb{Q}_{BA}, \mathbb{X}])_{la,la} \}, \quad (22)$$

Here, \mathbb{X} is the position operator. \mathbb{Q} can be defined from the modal matrix \mathbb{U} , which is comprised of all the normalized eigen vectors with ascending order, explicitly, $\mathbb{U} = [\mathbb{U}_1, \mathbb{U}_2, \dots, \mathbb{U}_n, \mathbb{U}_{n+1}, \dots, \mathbb{U}_N]$. Here, $\mathbb{U}_- = [\mathbb{U}_1, \mathbb{U}_2, \dots, \mathbb{U}_n]$, and $\mathbb{U}_{+-} = [\mathbb{U}_{n+1}, \mathbb{U}_{n+2}, \dots, \mathbb{U}_N]$ are corresponds to below and above the band gap energy spectrum. Then one can define the projectors as $\mathbb{P}_- = \mathbb{U}_- \mathbb{U}_-^T$ and $\mathbb{P}_+ = \mathbb{U}_{+-} \mathbb{U}_{+-}^T$, and \mathbb{Q} as, $\mathbb{Q} = \mathbb{P}_+ - \mathbb{P}_-$, which further can be decomposed as, $\mathbb{Q} = \mathbb{Q}_{AB} + \mathbb{Q}_{BA} = \Gamma_A \mathbb{Q} \Gamma_B + \Gamma_B \mathbb{Q} \Gamma_A$, where $\Gamma = \Gamma_A - \Gamma_B$ is the chiral operator. More about the formula and the operators can be found in the appendix of [56, 57]. From the Figs. 6, 7, we observe that even for $\sigma = 1$, the LTM shows the same winding number for the both CST-SSH Hamiltonians as its usual SSH counterparts, for the exact values of the hopping. There is no apparent difference between the standard and the position-dependent hopping SSH models for this static marker, also indicating same topological phase boundaries for the CST models as well.

B. Mean Chiral Displacement

The previous topological measure was a static measure; in this section, we use a dynamical topological measure, which we call Mean Chiral Displacement (MCD) [56, 58], can be used to detect the winding number which is defined as,

$$C(\tau) = 2 \langle \psi(\tau) | \Gamma \mathbb{X} | \psi(\tau) \rangle, \quad (23)$$

where $|\psi(\tau)\rangle = e^{-iH\tau} |\psi_i\rangle$, i.e., $|\psi(\tau)\rangle$ is the time evolved state of an initially localized state at $n = N/2$ unit cell in the A sublattice, i.e., $|\psi_i\rangle$. Γ, \mathbb{X} are chiral and displacement operators, respectively. In the figure 8, we show the time-dependent MCD for both the trivial and topological phases, where it oscillates and converges to 0 in the case of a trivial phase and, on

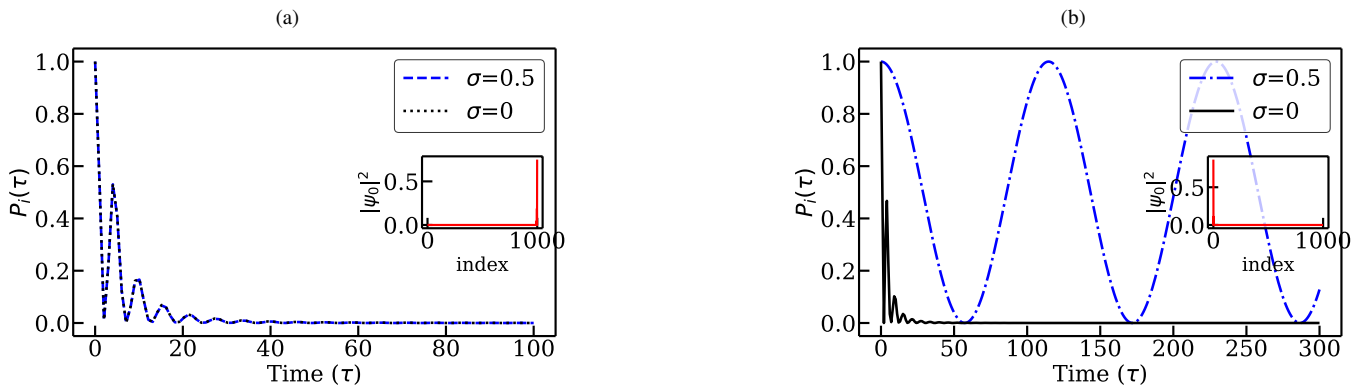


FIG. 9: Measurement of survival probability $P_i(t)$ from winding number 1 (with $(t_1, t_2, t_3, t_4) = (0.5, 1, 0, 0)$) to winding number 0 (with $(t_1, t_2, t_3, t_4) = (1, 0.5, 0, 0)$) for (a) right edge zero energy eigen state and, (b) left edge zero energy eigen state, for system size $2N = 1000$ (500 unit cells)

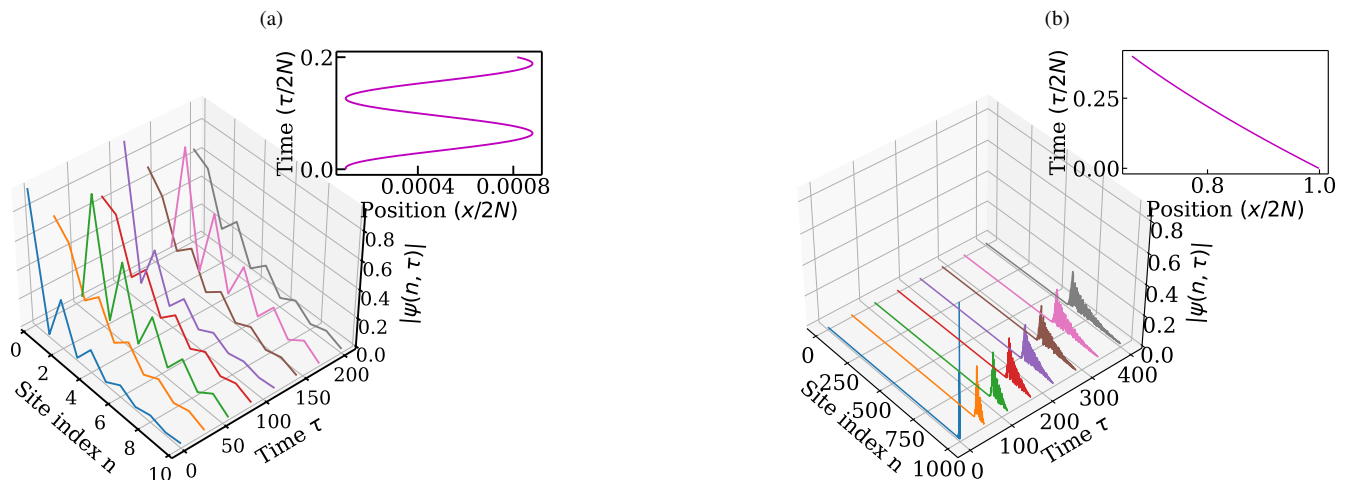


FIG. 10: Time evolution of the zero energy eigenstates for system size $2N = 1000$ (500 unit cells), : (a) left, and, (b) right edge zero energy eigenstate of a Hamiltonian with winding number 1, in another Hamiltonian with winding number zero. Inset of Fig. (a) shows the semiclassical dynamics near the origin, where the left edge state is located. Inset of Fig. (b) shows the semiclassical dynamics where the right edge state is located.

the other hand, saturates to 1 in the case of a topological phase for the usual SSH model. On the other hand, for $\sigma \neq 0$ also, the MCD oscillates around its respective winding number, but the fluctuations are much higher compared to $\sigma = 0$, though the average MCD remains the same. Overall, the MCD results complement our previous results for the static measure. This indeed proves that, like the usual SSH models, even the CST-SSH models display topologically distinct phases corresponding to distinct winding numbers for the same conditions on the hopping as the regular SSH models, though the model remains gapless even away from the topological transition points for $\sigma \geq 1$.

VI. QUENCH DYNAMICS: FROM TOPOLOGICAL TO TRIVIAL PHASE

In this section, we study the quench dynamics across the topological transition point. For the sake of numerical simplicity and understanding the mechanism better, we study the dynamics in the limit of $t_3 = t_4 = 0$, leaving the Hamiltonian with two possible winding numbers: 0, 1. We prepare our initial state $|\psi_i\rangle$ as one of the zero-energy eigenstates of the CST-SSH Hamiltonian for $t_2 > t_1$. Note, this is the topologically non-trivial phase, having two edge modes. Then, we quench across the transition point in the topologically trivial phase. It implies $t_2 < t_1$ for the post-quench Hamiltonian, which we identify as H_f . The survival probability of the initial state after

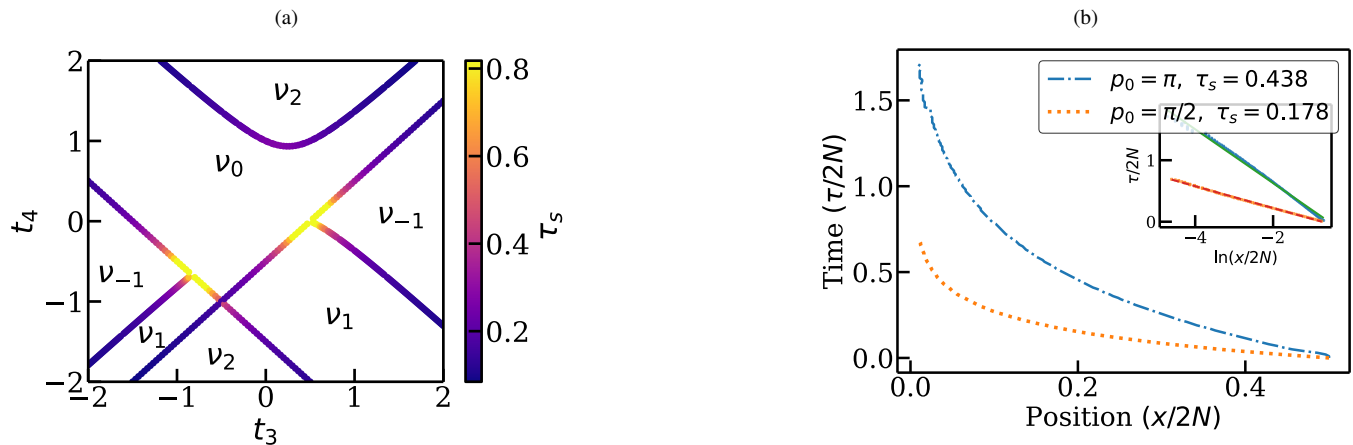


FIG. 11: (a) Values of slowdown time scale τ_s with $t_1 = 1, t_2 = 0.5$ and over range of t_3, t_4 . Here $v_i, (i = -1, 0, 1, 2)$ represent regions with winding number i . (b) for a higher order gap closing point $(1, 0.5, -0.5, -1)$, two different critical slowdown parameters τ_s for two initial critical momenta, inset plot showing a Log-linear plot of the same, with straight-line fits used to extract τ_s for each p_0 , For system size $2N = 1000$ (500 unit cells):

quench is given by [59, 60],

$$P_i(\tau) = |\langle \psi_i | e^{-iH_f \tau} | \psi_i \rangle|^2. \quad (24)$$

It is basically a measurement of the likelihood of the zero-energy eigenstate of a topologically nontrivial Hamiltonian remaining the same after the unitary time evolution of the state in another Hamiltonian with winding number 0. Although the topological markers produce nearly identical results for the CST-SSH and the conventional SSH models, we had identified a clear asymmetry in the edge modes of the CST-SSH model, unlike the identical edge modes of the usual SSH model. In this section, our goal is to examine how these asymmetric edge modes evolve under our quench protocol. By contrast, in the usual SSH model the symmetric edge modes are expected to exhibit identical dynamics under the same protocol.

Figure. 9 shows the variation of the survival probability with time for the usual SSH model, i.e., $\sigma = 0$, and for the CST-SSH model with $\sigma = 0.5$. We quench from $(t_1, t_2) = (0.5, 1)$ to $(t_1, t_2) = (1, 0.5)$. For the initial state, i.e., localized at the right edge, the time evolution of the survival probability is almost identical for the usual SSH and the CST-SSH model (see Fig. 9a). The survival probability goes to zero reasonably quickly. However, the dynamics are quite different between these two models for the left edge mode (see Fig. 9b). While for the usual SSH, the dynamic is almost indistinguishable from that obtained for the right edge mode, for $\sigma > 0$, the survival probability seems to oscillate between 0 and 1 for the CST-SSH model. We find that the oscillation period increases with increasing σ . The fact that dynamics is identical for usual SSH and not for CST-SSH is not too surprising, given that we found in Sec. IV that both edge states are symmetric for $\sigma = 0$, and asymmetry kicks in as soon as $\sigma > 0$. However, it still does not explain why the survival probability of the left-edge states oscillates. Hence, we plot the absolute value of the time-evolved wavefunction in Fig. 10, and find that for the CST-SSH model, while under time evolution,

the right edge state moves toward the other side of the lattice, while the left edge mode kind of remains there. If one tracks the peak position, one finds that it moves a bit to the right and then again comes back, keeping up this to-and-fro motion. This is precisely what gets manifested in the survival probability plot. Moreover, we find the same picture even when solving the semi-classical equation of motion (see inset of Fig. 10).

VII. QUANTIFICATION OF THE CRITICAL SLOWDOWN

At this point, we have established that there exists a connection between the topological transition points in SSH models and the observation of horizon physics in their CST counterparts. Unlike the standard SSH model, the extended SSH model supports higher-order topological phases. While obtaining the semiclassical trajectories of the wave packets, we observed that at different topological phase transition points the rate at which the wave packet approaches the origin varies across the hopping parameter space. Therefore, in this section we quantify the slowdown rate by introducing a characteristic time scale, τ_s , which allows us to better understand the horizon physics in topological systems with multiple gap-closing constraints for usual extended SSH models. During the critical slowdown, the peak position of the wave packet follows

$$x(\tau) = x_0 e^{-\tau/\tau_s}, \quad (25)$$

as shown in Fig. 11b. Thus, for a chosen range of initial hopping parameters, we can analyze how fast or slow the wave packet moves toward the origin. Figure 11a shows the different winding numbers and the transition lines separating the topological phases. The heatmap indicates how slowly the wave packet moves toward the origin: larger values of τ_s correspond to slower motion. We observe that the horizon

physics, characterized by the critical slowdown, appears only along the transition lines.

In our calculations we fix $t_1 = 1$ and $t_2 = 0.5$, and compute the slowdown parameter τ_s over a range of t_3 and t_4 . We find that when condition (iii) and either condition (i) or (ii) of Eq. 5 are satisfied simultaneously, the wave packet does not evolve with time and effectively becomes stationary. The reason is that satisfying two gap-closing conditions at the same Dirac point makes the initial group velocity vanish. In the vicinity of these stationary points, the value of τ_s becomes larger, implying that the wave packets approach the origin more slowly compared to other transition points where only a single gap-closing constraint is satisfied. This behavior is visible in Fig. 11a as the bright yellow regions near the junctions. We also observe another interesting phenomenon. At higher-order gap-closing points of the usual extended SSH model where both conditions (i) and (ii) of Eq. 5 are satisfied, two different critical slowdowns emerge for two different initial momenta p_0 , resulting in two distinct slowdown parameters τ_s (see Fig. 11b). Such features arise only in topological systems with higher-order gap closings, such as the extended CST-SSH model. Note that we would like to clarify that whenever we refer to gap-closing points in this section, we mean the gap-closing points of the usual extended SSH model at the topological transition points, and not those of the CST-SSH model. This distinction is important because the CST-SSH model remains gapless for $\sigma \geq 1$, as discussed previously. Finally, this provides an additional degree of freedom to control the critical slowdown in experimental setups designed to mimic black hole horizon physics. Such flexibility is absent in the simpler CST-SSH model.

VIII. SUMMARY AND DISCUSSION

In this paper, we investigate the topological properties of both the extended and standard version of CST-SSH model. We find that, for both model, the physics of the event horizon manifests only at the topological phase transition points, where a critical slowdown occurs for zero-energy wave packets near the boundary. The wave-packet dynamics results are also supported by an analytical calculation of semiclassical trajectories. We analyze the energy spectrum and find that when the intercell hopping is larger than the intracell hopping, a pair of zero-energy states emerges. These states are localized at the two edges of the lattice. However, unlike in the conventional SSH model, these edge states are not symmetric. We also find that, similar to the usual SSH model, the spectrum exhibits a gap whenever the intra- and inter-cell hopping amplitudes are unequal. However, this gap scales to zero with system size as $N^{-\sigma}$. Since the typical gap of a finite-size system scales as N^{-1} , it implies that for $\sigma < 1$ the spectrum remains gapped in the thermodynamic limit [52], and gapless for $\sigma \geq 1$. Moreover, we use various real-space topological markers, both static and dynamic, which show a clear signature of a topological phase transition for the CST-SSH models between a topologically trivial phase and a non-trivial phase

for the exact parameters, as the usual SSH models. Even though the spectrum remains gapless away from the transition points for $\sigma \geq 1$, these regions do not exhibit horizon physics. This shows that the mere gaplessness of the spectrum is not sufficient for the emergence of horizon physics. Instead, the gapless points corresponding to topological transitions are special, as they support the critical slowdown associated with horizon physics. This observation naturally raises a fundamental question: how can one define a topological marker that characterizes transitions between phases that remain gapless in the CST versions of SSH-type models? Despite the introduction of power law position dependent hopping, we show that the symmetry class of the CST-SSH models remain in BDI category. Moreover, it turns out that although the spectrum is gapless, the states in the neighborhood of the zero-energy modes are spatially localized (see Appendix A). This localization is likely the reason why the system retains its topological character. Effectively, a mobility gap emerges in the system. In other words, the zero-energy states are surrounded by localized states that do not contribute to transport, making the system effectively insulating. Such phenomena are typically observed in disordered topological systems [49, 50]. Even very recently, such phenomena have been reported in disordered SSH models, where, in contrast to the conventional SSH model, the topological transition points separate two gapless phases [51]. We also study the quench dynamics from topological to trivial state and explain the oscillatory behavior of the survival probability with our semiclassical calculations. Further, analyze the slowdown quantification for the extended CST-SSH, and found that, in the vicinity of the higher order gap closing points, where two gap closing conditions for the conventional extended SSH models are satisfied for the same k_c value, the slowdown rate is higher. Also, for the other higher order gap closing points, where two gap closing conditions are satisfied for two different k_c values, we observe that there are two distinct values of p_0 ($= \pi, \pi/2$), having two critical slowdown with different τ_s , for the same set of hopping parameters. With the advancement of cold-atom experiments, there is potential for our predictions to be verified in the near future [61–63], which could enrich our understanding of both black hole physics and inhomogeneous topological systems.

ACKNOWLEDGMENTS

R.M. acknowledges the DST-Inspire fellowship by the Department of Science and Technology, Government of India, SERB start-up grant (SRG/2021/002152).

Appendix A: Zero energy and its neighboring states of the extended CST-SSH Model

In this section, we discuss both the energy band closing and the zero-energy edge states in the extended CST-SSH model. For the Hamiltonian 4, we observe various winding numbers:

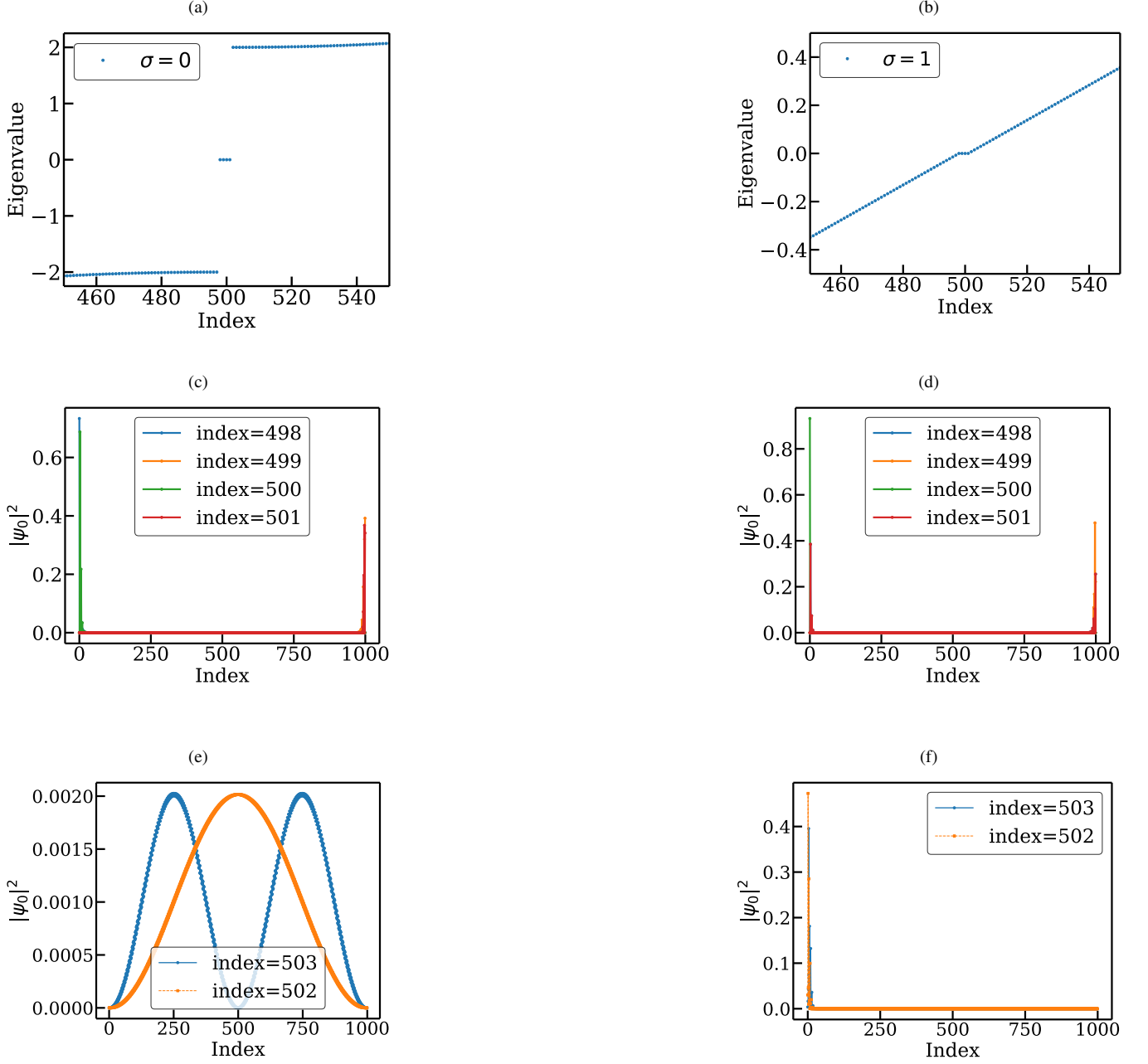


FIG. 12: Closing of the energy band gap and variation of zero energy eigen states variation with σ : for the extended CST-SSH model having system size $2N = 1000$ (500 unit cells) with $(t_1, t_2, t_3, t_4) = (2, 1, -1, -4)$, which have a winding number 2. Top row (a),(b): Eigenvalue spectra for $\sigma=0$ and 1, respectively. Bottom row (c),(d): Corresponding zero-energy eigenstates profiles. (e),(f): probability densities for non-zero eigen energies for (e) $\sigma = 0$, (f) $\sigma = 1$

specifically $-1, 0, 1$, and 2 , which can be realized by appropriately tuning the parameters (t_1, t_2, t_3, t_4) . Here, the winding number corresponds to the number of zero-energy edge modes per boundary under open boundary conditions.

For example, in Fig. 12, we choose $(t_1, t_2, t_3, t_4) = (2, 1, -1, -4)$, which yields a winding number of two. This is evident from the presence of two zero-energy edge states per

boundary, observed for both $\sigma = 0$ and $\sigma = 1$. Figs. 12e, 12f shows the probability densities corresponding to two states near to the zero energy eigen states. For $\sigma = 0$, they are delocalized; but at $\sigma = 1$, these states become localized near the edge. The model can be further extended or modified to realize higher winding numbers.

As discussed in the main text, the energy gap in the extended

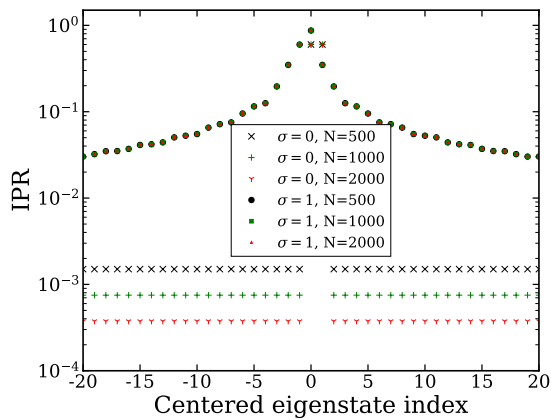


FIG. 13: IPR of the eigen states of the near zero energy neighborhood, for $\sigma = 0, 1$ for different system sizes with $(t_1, t_2, t_3, t_4) = (0.5, 1, 0, 0)$,

model gradually closes as a function of σ , and one of the zero-energy edge states become more localized. However, the application of σ does not alter the winding number, which was demonstrated in the Fig.6. We also study the wavefunctions

of the states in the neighborhood of the zero-energy localized states (Fig. 12f) and find that, for the CST-SSH model, the probability densities corresponding to these states are also spatially localized. To probe more into these localized states, we also calculated the Inverse Participation ratio (IPR) for the states in the neighborhood of the zero energy states. To quantify the degree of localization of an eigenstate $|\psi\rangle = \sum_i \psi_i |i\rangle$, we compute the inverse participation ratio (IPR), defined as [64]

$$\text{IPR} = \sum_i |\psi_i|^4, \quad (\text{A1})$$

for which larger values indicate stronger spatial localization. The Fig. 13 shows the IPR for various system sizes and for $\sigma = 0, 1$. For $\sigma = 0$, IPR decreases as we increase the system size (except the two zero energy states at the centre), implying the eigenstates are delocalized (except the zero energy states). For $\sigma = 1$, the states around zero energy, with increasing the system size, have the same IPR values, thus confirming that these zero energy and even their neighborhood states are localized. As a result, these states do not contribute to transport and effectively act as a mobility gap, even though the spectrum itself remains gapless. This behavior is absent in the $\sigma = 0$ case.

-
- [1] A. Einstein, Die grundlage der allgemeinen relativitätstheorie [adp 49, 769 (1916)], Annalen der Physik **517**, 517 (2005).
- [2] W. G. Unruh, Experimental black-hole evaporation?, Physical Review Letters **46**, 1351 (1981).
- [3] R. Schützhold and W. G. Unruh, Gravity wave analogues of black holes, Phys. Rev. D **66**, 044019 (2002).
- [4] G. E. Volovik, Superfluid analogies of cosmological phenomena, Physics Reports **351**, 195 (2001).
- [5] M. Novello, V. De Lorenci, J. Salim, and R. Klippert, Geometrical aspects of light propagation in nonlinear electrodynamics, Physical Review D **61**, 045001 (2000).
- [6] M. Novello and J. Salim, Effective electromagnetic geometry, Physical Review D **63**, 083511 (2001).
- [7] B. Reznik, Origin of the thermal radiation in a solid-state analogue of a black hole, Physical Review D **62**, 044044 (2000).
- [8] R. Schützhold, G. Plunien, and G. Soff, Dielectric black hole analogs, Physical review letters **88**, 061101 (2002).
- [9] O. Lahav, A. Itah, A. Blumkin, C. Gordon, S. Rinott, A. Zayats, and J. Steinhauer, Realization of a sonic black hole analog in a bose-einstein condensate, Phys. Rev. Lett. **105**, 240401 (2010).
- [10] L. J. Garay, J. R. Anglin, J. I. Cirac, and P. Zoller, Sonic analog of gravitational black holes in bose-einstein condensates, Phys. Rev. Lett. **85**, 4643 (2000).
- [11] A. J. Kollár, M. Fitzpatrick, and A. A. Houck, Hyperbolic lattices in circuit quantum electrodynamics, Nature **571**, 45 (2019).
- [12] H. S. Nguyen, D. Gerace, I. Carusotto, D. Sanvitto, E. Galopin, A. Lemaître, I. Sagnes, J. Bloch, and A. Amo, Acoustic black hole in a stationary hydrodynamic flow of microcavity polaritons, Phys. Rev. Lett. **114**, 036402 (2015).
- [13] B. Lapierre, K. Choo, C. Tauber, A. Tiwari, T. Neupert, and R. Chitra, Emergent black hole dynamics in critical floquet systems, Phys. Rev. Res. **2**, 023085 (2020).
- [14] B. Lapierre, T. Numasawa, T. Neupert, and S. Ryu, Floquet engineered inhomogeneous quantum chaos in critical systems (2024), arXiv:2405.01642 [cond-mat.str-el].
- [15] U. R. Fischer and R. Schützhold, Quantum simulation of cosmic inflation in two-component bose-einstein condensates, Phys. Rev. A **70**, 063615 (2004).
- [16] P. O. Fedichev and U. R. Fischer, Gibbons-hawking effect in the sonic de sitter space-time of an expanding bose-einstein-condensed gas, Phys. Rev. Lett. **91**, 240407 (2003).
- [17] Z. Tian, Y. Lin, U. R. Fischer, and J. Du, Testing the upper bound on the speed of scrambling with an analogue of hawking radiation using trapped ions, The European Physical Journal C **82**, 10.1140/epjc/s10052-022-10149-8 (2022).
- [18] C. C. H. Ribeiro, S.-S. Baak, and U. R. Fischer, Existence of steady-state black hole analogs in finite quasi-one-dimensional bose-einstein condensates, Phys. Rev. D **105**, 124066 (2022).
- [19] S. Sachdev and J. Ye, Gapless spin-fluid ground state in a random quantum heisenberg magnet, Phys. Rev. Lett. **70**, 3339 (1993).
- [20] J. Maldacena and D. Stanford, Remarks on the sachdev-ye-kitaev model, Phys. Rev. D **94**, 106002 (2016).
- [21] A. Kitaev and S. J. Suh, The soft mode in the sachdev-ye-kitaev model and its gravity dual, Journal of High Energy Physics **2018**, 1 (2018).
- [22] S.-Z. Li, X.-J. Yu, S.-L. Zhu, and Z. Li, Anderson localization and swing mobility edge in curved spacetime, Physical Review B **108**, 094209 (2023).
- [23] L. Mertens, A. G. Moghaddam, D. Chernyavsky, C. Morice, J. van Den Brink, and J. van Wezel, Thermalization by a synthetic horizon, Physical Review Research **4**, 043084 (2022).
- [24] C. Morice, D. Chernyavsky, J. van Wezel, J. van den Brink, and A. Moghaddam, Quantum dynamics in 1d lattice models with synthetic horizons, SciPost Physics Core **5**, 042 (2022).

- [25] C. Morice, A. G. Moghaddam, D. Chernyavsky, J. van Wezel, and J. van den Brink, Synthetic gravitational horizons in low-dimensional quantum matter, *Physical Review Research* **3**, L022022 (2021).
- [26] D. J. Thouless, M. Kohmoto, M. P. Nightingale, and M. den Nijs, Quantized hall conductance in a two-dimensional periodic potential, *Phys. Rev. Lett.* **49**, 405 (1982).
- [27] C. L. Kane and E. J. Mele, Quantum spin hall effect in graphene, *Phys. Rev. Lett.* **95**, 226801 (2005).
- [28] L. Fu, C. L. Kane, and E. J. Mele, Topological insulators in three dimensions, *Phys. Rev. Lett.* **98**, 106803 (2007).
- [29] B. A. Bernevig, T. L. Hughes, and S.-C. Zhang, Quantum spin hall effect and topological phase transition in hgte quantum wells, *science* **314**, 1757 (2006).
- [30] D. Hsieh, D. Qian, L. Wray, Y. Xia, Y. S. Hor, R. J. Cava, and M. Z. Hasan, A topological dirac insulator in a quantum spin hall phase, *Nature* **452**, 970 (2008).
- [31] Y. Chen, J. G. Analytis, J.-H. Chu, Z. Liu, S.-K. Mo, X.-L. Qi, H. Zhang, D. Lu, X. Dai, Z. Fang, et al., Experimental realization of a three-dimensional topological insulator, *bi2te3*, *science* **325**, 178 (2009).
- [32] C.-Z. Chang, J. Zhang, X. Feng, J. Shen, Z. Zhang, M. Guo, K. Li, Y. Ou, P. Wei, L.-L. Wang, et al., Experimental observation of the quantum anomalous hall effect in a magnetic topological insulator, *Science* **340**, 167 (2013).
- [33] L. Fu, Topological crystalline insulators, *Phys. Rev. Lett.* **106**, 106802 (2011).
- [34] Y. Tanaka, Z. Ren, T. Sato, K. Nakayama, S. Souma, T. Takahashi, K. Segawa, and Y. Ando, Experimental realization of a topological crystalline insulator in *snTe*, *Nature Physics* **8**, 800 (2012).
- [35] P. Dziawa, B. Kowalski, K. Dybko, R. Buczko, A. Szczerbakow, M. Szot, E. Lusakowska, T. Balasubramanian, B. M. Wojek, M. Berntsen, et al., Topological crystalline insulator states in *pb1-x sn x se*, *Nature materials* **11**, 1023 (2012).
- [36] A. A. Burkov and L. Balents, Weyl semimetal in a topological insulator multilayer, *Phys. Rev. Lett.* **107**, 127205 (2011).
- [37] A. A. Burkov and L. Balents, Weyl semimetal in a topological insulator multilayer, *Phys. Rev. Lett.* **107**, 127205 (2011).
- [38] S. Borisenko, Q. Gibson, D. Evtushinsky, V. Zabolotnyy, B. Büchner, and R. J. Cava, Experimental realization of a three-dimensional dirac semimetal, *Phys. Rev. Lett.* **113**, 027603 (2014).
- [39] H. Watanabe, H. C. Po, M. P. Zaletel, and A. Vishwanath, Filling-enforced gaplessness in band structures of the 230 space groups, *Phys. Rev. Lett.* **117**, 096404 (2016).
- [40] W.-P. Su, J. Schrieffer, and A. Heeger, Soliton excitations in polyacetylene, *Physical Review B* **22**, 2099 (1980).
- [41] H. Takayama, Y. R. Lin-Liu, and K. Maki, Continuum model for solitons in polyacetylene, *Phys. Rev. B* **21**, 2388 (1980).
- [42] S. Kivelson and D. E. Heim, Hubbard versus peierls and the su-schrieffer-heeger model of polyacetylene, *Phys. Rev. B* **26**, 4278 (1982).
- [43] A. J. Heeger, S. Kivelson, J. R. Schrieffer, and W. P. Su, Solitons in conducting polymers, *Rev. Mod. Phys.* **60**, 781 (1988).
- [44] D. Joshi and T. Nag, Adiabatic charge transport in extended ssh models, *arXiv preprint arXiv:2503.18125* (2025).
- [45] E. J. Meier, F. A. An, and B. Gadway, Observation of the topological soliton state in the su-schrieffer-heeger model, *Nature communications* **7**, 13986 (2016).
- [46] C. Morice, D. Chernyavsky, J. van Wezel, J. van den Brink, and A. Moghaddam, Quantum dynamics in 1d lattice models with synthetic horizons, *SciPost Physics Core* **5**, 10.21468/scipostphyscore.5.3.042 (2022).
- [47] C. Y. Wong, T. H. Hui, P. D. Sacramento, and W. C. Yu, Entanglement in quenched extended su-schrieffer-heeger model with anomalous dynamical quantum phase transitions, *Phys. Rev. B* **110**, 054312 (2024).
- [48] G. Jin, D. O. Oriekhov, L. J. Splitthoff, and E. Greplova, Topological finite size effect in one-dimensional chiral symmetric systems (2024), *arXiv:2411.17822 [cond-mat.mes-hall]*.
- [49] Y.-Y. Zhang, R.-L. Chu, F.-C. Zhang, and S.-Q. Shen, Localization and mobility gap in the topological anderson insulator, *Phys. Rev. B* **85**, 035107 (2012).
- [50] D. Xu, J. Qi, J. Liu, V. Sacksteder, X. C. Xie, and H. Jiang, Phase structure of the topological anderson insulator, *Phys. Rev. B* **85**, 195140 (2012).
- [51] S. Mondal and A. Agarwala, Topological phase transition under infinite randomness (2025), *arXiv:2506.19913 [cond-mat.dis-nn]*.
- [52] T. Mishra, J. Carrasquilla, and M. Rigol, Phase diagram of the half-filled one-dimensional $t-v-V'$ model, *Phys. Rev. B* **84**, 115135 (2011).
- [53] J. K. Asbóth, L. Oroszlány, and A. Pályi, *A Short Course on Topological Insulators* (Springer International Publishing, 2016).
- [54] A. Altland and M. R. Zirnbauer, Nonstandard symmetry classes in mesoscopic normal-superconducting hybrid structures, *Physical Review B* **55**, 1142-1161 (1997).
- [55] S. Ryu, A. P. Schnyder, A. Furusaki, and A. W. W. Ludwig, Topological insulators and superconductors: tenfold way and dimensional hierarchy, *New Journal of Physics* **12**, 065010 (2010).
- [56] X. Shi, I. Kiopelidis, R. Chaunsali, V. Achilleos, G. Theocharis, and J. Yang, Disorder-induced topological phase transition in a one-dimensional mechanical system, *Phys. Rev. Res.* **3**, 033012 (2021).
- [57] E. J. Meier, F. A. An, A. Dauphin, M. Maffei, P. Massignan, T. L. Hughes, and B. Gadway, Observation of the topological anderson insulator in disordered atomic wires, *Science* **362**, 929 (2018).
- [58] F. Cardano, A. D'Errico, A. Dauphin, M. Maffei, B. Piccirillo, C. de Lisio, G. De Filippis, V. Cataudella, E. Santamato, L. Marrucci, M. Lewenstein, and P. Massignan, Detection of zak phases and topological invariants in a chiral quantum walk of twisted photons, *Nature Communications* **8**, 10.1038/ncomms15516 (2017).
- [59] A. Ghosh, A. M. Martin, and S. Majumder, Quench dynamics of edge states in a finite extended su-schrieffer-heeger system, *Phys. Rev. E* **108**, 034102 (2023).
- [60] M. Suman, S. Aravinda, and R. Modak, Probing quantum phase transitions via quantum speed limits, *Phys. Rev. A* **110**, 012466 (2024).
- [61] D.-W. Zhang, Y.-Q. Zhu, Y. Zhao, H. Yan, and S.-L. Zhu, Topological quantum matter with cold atoms, *Advances in Physics* **67**, 253 (2018).
- [62] C. Viermann, M. Sparn, N. Liebster, M. Hans, E. Kath, Á. Parra-López, M. Tolosa-Simeón, N. Sánchez-Kuntz, T. Haas, H. Strobel, et al., Quantum field simulator for dynamics in curved spacetime, *nature* **611**, 260 (2022).
- [63] C. Barceló, Analogue black-hole horizons, *Nature Physics* **15**, 210 (2019).
- [64] J. Jeon, H. Ikeda, and S. Sakai, Delocalization induced by enhanced hyperuniformity in one-dimensional disordered systems, *Phys. Rev. B* **113**, L020201 (2026).
- [65] L. Viotti, A. L. Gramajo, P. I. Villar, F. C. Lombardo, and R. Fazio, Geometric phases along quantum trajectories, *Quantum* **7**, 1029 (2023).

- [66] V. Könye, C. Morice, D. Chernyavsky, A. G. Moghaddam, J. van den Brink, and J. van Wezel, Horizon physics of quasi-one-dimensional tilted weyl cones on a lattice, *Phys. Rev. Res.* **4**, 033237 (2022).
- [67] L. Mertens, A. G. Moghaddam, D. Chernyavsky, C. Morice, J. van den Brink, and J. van Wezel, Thermalization by a synthetic horizon, *Phys. Rev. Res.* **4**, 043084 (2022).
- [68] R. He, Y. Zhao, C. Sheng, J. Duan, Y. Wei, C. Sun, L. Lu, Y.-X. Gong, S. Zhu, and H. Liu, Experimental realization of quantum walks near synthetic horizons on photonic lattices, *Phys. Rev. Res.* **6**, 013233 (2024).
- [69] C. D. Beule, S. Groenendijk, T. Meng, and T. L. Schmidt, Artificial event horizons in Weyl semimetal heterostructures and their non-equilibrium signatures, *SciPost Phys.* **11**, 095 (2021).
- [70] A. G. Moghaddam, D. Chernyavsky, C. Morice, J. van Wezel, and J. van den Brink, Engineering spectral properties of non-interacting lattice Hamiltonians, *SciPost Phys.* **11**, 109 (2021).